Journal Name

ARTICLE TYPE

Cite this: DOI: 00.0000/xxxxxxxxxx

A Data-Mining Approach to Understanding the Impact of Multi-doping on the Ionic Transport Mechanism of Solid Electrolytes Materials: The Case of Dual-doped $Ga_{0.15}/Sc_y$ $Li_7La_3Zr_2O_{12}$ †

Henry A. Cortés,*[a] Mauricio R. Bonilla,[a] Herbert Früchtl,[b] Tanja van Mourik,[b] Javier Carrasco,[c,d] and Elena Akhmatskaya[a,d]

Received Date
Accepted Date

DOI: 00.0000/xxxxxxxxxx

This study presents novel computational methods applied to the technologically significant solid electrolyte materials, $Li_{6.55+y}Ga_{0.15}La_3Zr_{2-y}Sc_yO_{12}$ ($Ga_{0.15}/Sc_y$-LLZO), in order to investigate the effect of the distribution of Ga^{3+} on Li-ion dynamics. Utilizing a specifically designed first-principles-based force field, molecular dynamics, and advanced hybrid Monte Carlo simulations, we systematically examine the material's transport properties for a range of Ga^{3+} and Sc^{3+} cationic concentrations. Additionally, we introduce innovative post-processing methods employing data mining clustering techniques, shedding light on Li^+ ion behavior and conductivity mechanisms. Contrary to prior assumptions, the presence of Ga^{3+} in octahedral sites, not tetrahedral junctions, optimally enhances Li-ion conductivity, unlocking Li-ion diffusion pathways. The research illuminates how dopant distribution influences Li^+ site occupancy and conductivity, offering key insights for advanced solid electrolyte design.

1 Introduction

The burgeoning growth in electromotive vehicles and intermittent energy generation from renewable sources is boosting the demand for safe, efficient, and cost-effective batteries[1]. Solid-State Batteries (SSBs) incorporating non-flammable, non-toxic, fast-ion conducting solid-state electrolytes (SSEs) hold immense potential towards satisfying these requirements[2,3]. Consequently, the search for suitable SSEs is a crucial aspect of SSB development. Various crystal structures, including perovskites, sulfides, NASICON-like and LISICON-like matrials, argyrodite and garnets[4,5], have emerged as promising candidates. Among these, $Li_7La_3Zr_2O_{12}$ (hereafter referred to as LLZO) garnet stands out due to its excellent lithium-ion conductivity (σ), wide electrochemical operation window, and its ability to form stable interfaces with many cathode materials[5].

Two distinct polymorphs of LLZO have been reported: a tetragonal phase ($I4_1/acd$, Space Group no. 142) with low conductivity and a highly conductive cubic phase ($Ia\bar{3}d$, Space Group no. 230), which is thermodynamically stable above 400-625 K (the exact value depends on the sample's impurity level)[6,7]. Tetragonal LLZO exhibits an ordered and fully occupied distribution of Li^+ ions. In contrast, cubic LLZO displays a disordered and partially occupied distribution of Li^+ ions between two types of Li-sites: the 24d tetrahedral (T_d) and the 48g/96h octahedral (O_h) sites (Figure 1). As a consequence, the cubic phase's conductivity surpasses that of its tetragonal counterpart by about two orders of magnitude at room temperature (RT)[8,9]. Within the Li^+ ion percolation network of cubic LLZO, T_d sites act as junctions connecting four neighboring O_h sites, while O_h sites only share faces with two T_d sites[8,10]. This suggests that the blocking of T_d junctions significantly impedes the connectivity of the Li^+ ion sublattice[10–12].

In recent years, research has focused on various substitution strategies to stabilize the cubic phase of LLZO at RT. Notable examples include ion substitutions such as Li^+ by Al^{3+}[12,13] or Ga^{3+}[10,14,15]; Zr^{4+} by Ta^{5+}[16] or Bi^{5+}[17]; as well as La^{3+} by Ca^{2+}, Sr^{2+} or Ba^{2+}[18]. Moreover, multi-ion substitutions have been

[a] Basque Center for Applied Mathematics (BCAM), Alameda de Mazarredo 14, E-48009 Bilbao, Spain. E-mail: hacortes@bcamath.org, mrincon@bcamath.org, eakhmatskaya@bcamath.org

[b] EaStCHEM School of Chemistry, University of St Andrews, St. Andrews KY16 9ST, United Kingdom. E-mail: herbert.fruchtl@st-andrews.ac.uk, tanja.vanmourik@st-andrews.ac.uk

[c] Centre for Cooperative Research on Alternative Energies (CIC energiGUNE), Basque Research and Technology Alliance (BRTA), Alava Technology Park, Albert Einstein 48, 01510, Vitoria-Gasteiz, Spain. E-mail:jcarrasco@cicenergigune.com

[d] IKERBASQUE, Basque Foundation for Science, Plaza Euskadi 5, 48009 Bilbao, Spain.

† Electronic Supplementary Information (ESI) available: Force field database and validation; Site analysis methodology validation; $Ga_{0.15}/Sc_y$-LLZO conventional ionic conductivity; $Ga_{0.15}/Sc_y$-LLZO occupancy limits; $Ga_{0.15}/Sc_{0.0}$-LLZO density maps. See DOI: 00.0000/00000000.

explored, aiming to stabilize the cubic phase with one dopant, while utilizing others to fine-tune the Li-molar content, crystal lattice size, and pellet densification [11,19–26]. For instance, Kang and coworkers [11] shifted the preferred site of Al^{3+} from 24d T_d to 96h O_h through the addition of Ta^{5+} as a co-dopant in the Zr^{4+} site, reducing the blocking of 24d T_d junctions and enhancing Li^+ diffusivity. Buannic *et al.* [19] employed a dual substitution approach with Ga^{3+} in the Li^+ site and Sc^{3+} in the Zr^{4+} site, achieving one of the highest ionic conductivities observed to date (1.8×10^{-3} S/cm at RT) for the system $Li_{6.55+y}Ga_{0.15}La_3Zr_{2-y}Sc_yO_{12}$ at $y = 0.10$. This result was rationalized by arguing that Ga^{3+} stabilizes the cubic phase, while the presence of Sc^{3+} ($y > 0$) prompts an increase in the Li^+ content. Moreover, density functional theory (DFT) calculations and ^{71}Ga Nuclear Magnetic Resonance (NMR) measurements indicated that Sc^{3+} contents higher than $y = 0.10$ enabled preferential Ga^{3+} occupation of 48g/96h O_h sites over the 24d T_d sites. Although Buannic *et al.* suggested that this shift negatively impacted σ via the obstruction of the Li^+ percolation network [19], earlier studies have proposed that preferential doping on the O_h sites may actually benefit Li^+ diffusion by freeing T_d site junctions [11,12].

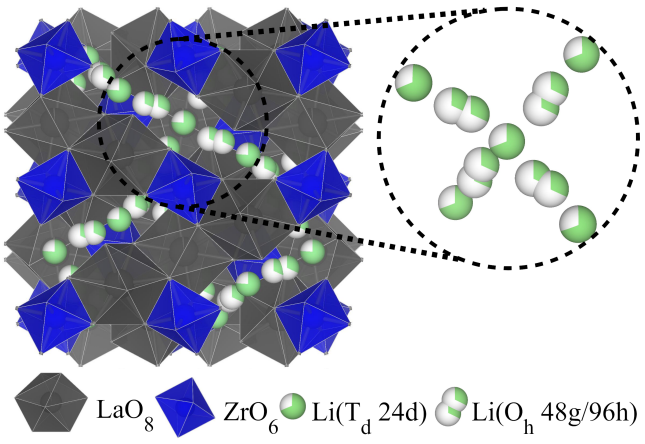

Fig. 1 Crystal structure of garnet-type cubic LLZO ($Ia\bar{3}d$ SG 230), with Li-ions represented by partially green filled spheres to indicate their partial occupancy. La^{3+} dodecahedra and Zr^{4+} octahedra are depicted in gray and blue, respectively. The Li-ion diffusion pathway comprises 24d tetrahedral (T_d) sites coordinated by four 48g/96h octahedral (O_h) sites.

From a computational viewpoint, in previous work, we investigated Al^{3+} and Ga^{3+}/Al^{3+} substitution strategies by assuming that both cations preferentially occupied T_d sites [27,28]. Furthermore, DFT analysis conducted by Buannic *et al.* on the dual-doped Ga^{3+}/Sc^{3+} garnet focused on a simplified system containing only one Ga^{3+} and one Sc^{3+} [19], which means that the potential impact of varying their concentration could not be systematically explored. Thus, the effect of the Sc^{3+} content, as well as the impact of Ga^{3+} distribution between O_h and T_d sites, have not been thoroughly addressed.

In this study, we delve into understanding the effect of Ga^{3+} distribution on Li^+ ion site occupancies, as well as the impact of Sc^{3+} co-doping on the Li^+ dynamics. To achieve this goal, we combine molecular dynamics (MD) and importance sampling hybrid Monte Carlo simulations, along with a novel material-specific first principles-based force field developed within this study. This approach enables us to accurately describe the ion dynamics in the $Li_{6.55+y}Ga_{0.15}La_3Zr_{2-y}Sc_yO_{12}$ ($Ga_{0.15}/Sc_y$-LLZO) system with y varying from 0.0 to 0.20 at 300K, as originally proposed experimentally by Buannic *et al.* [19].

In addition, we introduce two new approaches for the post-processing of MD trajectories in solid electrolyte materials that exploit available data mining (DM) clustering techniques. The first approach enables the identification of the fraction of mobile Li^+ ions that actively contribute to the overall σ, providing theoretical support to recent experimental findings challenging the conventional assumption that all ions contribute equally to conduction in garnets [29,30]. The second method harnesses DM-clustering to comprehensively characterize the spatial distribution, site volume, and occupation of diffusive species, which is a prevalent subject of interest in the literature [31–36]. In contrast to previous methodologies, the latter approach is a density-based technique [34] that enables the clear separation and identification of crystallographic sites. This distinction is unattainable with a traditional density map, primarily due to the overlap of densities from different crystallographic sites caused by ion diffusion. Furthermore, this method eliminates the necessity for prior knowledge of the material's crystal topology or interatomic distances [31,32,35], striking a balance between computational efficiency and accuracy.

The paper is structured as follows. First, the details of the force field development, our post-processing approaches, and the atomistic model for $Ga_{0.15}/Sc_y$-LLZO are provided. Subsequently, the calculated ionic conductivity for a set of $Ga_{0.15}/Sc_y$-LLZO systems is presented. Finally, the trend in experimental ionic conductivity is explained based on the analysis of the effect of the Ga^{3+} distribution and Sc^{3+} content on Li^+ ion dynamics. In contrast to the previous hypothesis [19], our findings reveal that σ reaches a maximum due to the Ga^{3+} presence in the O_h sites as opposed to the T_d junctions, thereby freeing Li diffusion pathways. Additionally, the substitution of Zr^{4+} with Sc^{3+} results in increased Li^+ concentration and promotes the occupancy of Ga^{3+} in the O_h sites, both of which are, in principle, positive effects. However, beyond $y = 0.10$, the reduction in Li^+ vacancies dramatically reduces the average hopping frequency, negatively impacting the diffusivity and leading to a progressive decrease in σ.

2 Methodology and Computational Details

2.1 Derivation of a first principle-based force field

The interatomic potential energy between atoms in cubic $Ga_{0.15}/Sc_y$-LLZO was calculated using the Coulomb-Buckingham interatomic potential U_{ij}:

$$U_{ij} = \frac{q_i q_j}{4\pi\varepsilon |r_{ij}|} + A_{ij}\, exp(-B_{ij}|r_{ij}|) - \frac{C_{ij}}{|r_{ij}|^6}, \qquad (1)$$

where ε is the vacuum permittivity, $|r_{ij}|$ is the distance between atoms i and j, q_i and q_j are their respective charges, and A_{ij}, B_{ij} and C_{ij} are the parameters of the Buckingham potential. The force field parameters were obtained through the force-matching algorithm [37] implemented in the *Potfit* code [38]. *Potfit* uses simu-

lated annealing to determine the set of parameters that optimally reproduces the forces, stresses, and energies from reference data obtained through *ab initio* calculations.

The configurations used to develop the force field database were computed using the plane wave DFT code VASP (version 6.3)[39]. The Perdew-Burke-Ernzerhof (PBE) generalized gradient approximation functional was employed[40] with a cut-off energy of 520 eV. The Nosé-Hoover thermostat was used to keep the temperature constant in the canonical ensemble (NVT) for the *ab initio* molecular dynamics (AIMD) simulations[41]. We used the 8-formula-unit ($Li_7La_3Zr_2O_{12}$) conventional supercell, with cubic symmetry group $Ia\bar{3}d$ (Space Group 230). The equilibrium lattice parameters of the cell were fixed to the experimental values reported in the ICSD (CC: 422259) by Awaka *et al.*[6] ($a = b = c = 12.9827$ Å and $\alpha = \beta = \gamma = 90^\circ$) while the internal atomic positions were allowed to relax to a force threshold of 0.02 eV Å^{-1}. We used a $2 \times 2 \times 2$ Γ-centered k-point mesh to sample the irreducible Brillouin zone.

In order to accurately capture the Li^+ dynamics and atomic distribution in the dual-doped $Ga_{0.15}/Sc_y$-LLZO system, 3049 atomic configurations were selected to build a comprehensive database from DFT calculations. The atomic configurations encompass energy minimizations of the ground state at a temperature $T = 0$ K and AIMD in the NVT ensemble at $T = 900$ and 1000 K. The obtained force field parameters A_{ij}, B_{ij}, and C_{ij} are listed in Table 1.

Table 1 Buckingham parameters for $Ga_{0.15}/Sc_y$-LLZO. For all atom pairs not in the table below, $A_{ij} = B_{ij} = C_{ij} = 0$

$i-j$	A_{ij}(eV)	B_{ij}(Å^{-}1)	C_{ij}(eVÅ^6)
$La^{2.1+}$-$O^{1.4-}$	11375.241	3.990	30.89
$Zr^{2.8+}$-$O^{1.4-}$	1558.116	3.311	0.00
$O^{1.4-}$-$O^{1.4-}$	13215.139	4.519	25.34
$Li^{0.7+}$-$O^{1.4-}$	1028.775	3.985	0.00
$Ga^{2.1+}$-$O^{1.4-}$	11359.299	4.828	0.00
$Sc^{2.1+}$-$O^{1.4-}$	1958.566	3.288	0.00

Section S1 of the Supporting Information (SI) provides additional information about the DFT database and the validation of the force field. Table S1 outlines the DFT structures within the database, while Figures S1(a) and S1(b) present a comparison between predicted and experimental lattice constants (a) and ionic conductivity of Ga_x-LLZO, as a function of x. Additionally, a similar comparative analysis for $Ga_{0.15}/Sc_y$-LLZO, as a function of y, is illustrated in Figure 3(a) and (b). In both cases, the force field matches well experimental values (more details are provided in the results section). The term $\%T_d$ denotes the percentage of Ga^{3+} ions in T_d sites, with the extreme cases $100\%T_d$ and $0\%T_d$ representing all Ga^{3+} ions placed in T_d and O_h sites, respectively.

2.2 Generation of $Ga_{0.15}/Sc_y$-LLZO configurations

We employed 3×3×3 LLZO supercells to generate $Ga_{0.15}/Sc_y$-LLZO structures, varying $(y_i)_{i=1...5}$ from 0.00 to 0.20. Specifically, 32 Ga^{3+} and varying numbers of Sc^{3+} ions (0, 11, 22, 32, and 43) were inserted into randomly selected Li^+ and Zr^{4+} sites, respectively. To preserve electroneutrality, two Li^+ ions per Ga^{3+} were removed, and one Li^+ ion per Sc^{3+} was added. This procedure was iterated 250,000 times, and the lowest energy structure for each y_i was selected for subsequent atomistic simulations. Additionally, we explored six different distributions of Ga^{3+} ions among T_d and O_h sites for each Sc^{3+} content.

2.3 Classical MD simulations

Two simulation methods were used: MD and the Generalized Shadow Hybrid Monte Carlo (GSHMC) method[42–44]. GSHMC is an importance sampling technique, utilizing modified Hamiltonians to achieve high acceptance rates. It partially refreshes momenta instead of fully resetting them between Monte Carlo (MC) steps, preserving dynamical information. Integrated into MultiHMC-GROMACS, a custom modification of the open-source MD package GROMACS version 4.5.4, GSHMC efficiently handles system equilibration.[45,46] Meanwhile, plain MD was used for the production runs, generating 30 ns trajectories with snapshots saved at 1 ps intervals.

Periodic boundary conditions were considered in all directions. The cutoff for van der Waals and Coulomb interactions (the latter evaluated through the particle mesh Ewald method) were set to 12 and 11 Å, respectively. The systems were first equilibrated for 10 ns in the NPT ensemble using the Parrinello-Rahman barostat[47] ($\tau_P = 1$ ps) at the target temperature and a pressure of 1 bar. The tunable input parameters in GSHMC (MD trajectories length ($L = 250$), time step ($\Delta t = 2$ fs), partial velocity update parameter ($\phi = 0.1$), and the order of the modified Hamiltonian (4th order)) were taken from previous works[27,28,45,46]. Moreover, GSHMC was combined with our two-stage-modified adaptive integration approach (MAIA)[48] for modified Hamiltonian MC methods, which enables sampling enhancement without additional computational costs. For the MD production runs, the standard velocity Verlet integrator was employed with a time step of 2 fs in the NVT ensemble, and the temperature was controlled using a velocity rescaling thermostat ($\tau_T = 0.1$ ps).

2.4 Post-processing Methodology

In this study, we propose a framework to evaluate multiple properties of the structure and dynamics of the Li^+ ions in $Ga_{0.15}/Sc_y$-LLZO that can be readily adapted for the analysis of other solid electrolytes.

2.4.1 Ion clustering

To understand the contribution of individual Li^+ ions to the overall conductivity, we clustered them according to their mobilities. This pre-classification also accelerates the calculation of certain properties, such as correlation factors or Van-Hove analysis, which may be highly time-consuming.

The clustering process was conducted using the k-means algorithm[49] as implemented in scikit-learn[50]. To characterize the mobility of ion i, we calculate its average displacement over the number of frames with respect to the starting position, $< d_i >$,

using

$$< d_i >= \sum_{j=1}^{n} \frac{1}{j} \left| r_i(j\Delta t) - r_i(0) \right|, \quad (2)$$

where $r_i(t)$ denotes the position of ion i at time t, Δt is the timestep, and n is the total number of frames in the trajectory. Notice that by using $< d_i >$ instead of the total displacement of ion i helps mitigate the potential misclassification of it as a low-mobility ion. This situation may arise because ion i might accidentally return to a position very close to its initial location by the end of the simulation, despite covering a significant volume within the simulation box.

The elbow method was used to define the number of clusters k (3 in total), which we refer to as Li_1^+, Li_2^+, and Li_3^+. A comprehensive description of the ion clustering approach can be found in Section S2 of the Supporting Information.

2.4.2 Site occupancy and distribution analysis

To characterize the crystallographic sites of diffusive ions, we proposed a new approach building upon the Density-based Clustering of Trajectories (DCT) method initially introduced by Chen *et al.*[34]. We enhanced this method by incorporating the Density-based Spatial Clustering of Applications with Noise (DBSCAN) algorithm,[51] as implemented in the sci-kit-learn library[50]. Additionally, we modified the algorithm to accommodate periodic boundary conditions (PBC). Our method offers several advantages, most notably, it requires minimal prior knowledge about the material's structure while retaining the capability to discern atomic sites with diverse geometries. Figure 2 provides an overview of the key stages forming the proposed DCT methodology.

As illustrated in Figure 2, the process commences by constructing a density map of cubic voxels from the MD trajectory, as shown in the top panel of Figure 2 (a voxel size vl = 0.2 Å was found to provide an adequate resolution for the current system). Subsequently, a minimum density threshold, ρ_{cut}, is introduced to correctly identify the crystallographic sites through the DBSCAN algorithm, which uses $\rho > \rho_{cut}$ as a descriptor to classify the voxels that will be included into the clustering procedure. Determining the appropriate value for ρ_{cut} can be intricate. A small ρ_{cut} results in connected regions, rendering them unsuitable for distinguishing the shape and volume of individual sites. Conversely, an excessively large ρ_{cut} can lead to clusters that are too small, potentially resulting in the loss of valuable information[34].

To address this limitation, we adopt the principle that each site type should exhibit a similar volume. That is, sites of the same type should have approximately the same number of voxels. Following this principle, we put forward an iterative process in which an initial ρ_{cut} is proposed, and those voxels for which $\rho > \rho_{cut}$ are clustered (cluster map). Each cluster corresponds to a tentative crystallographic site. These sites are then clustered based on their volume (i.e., cluster size), and the level of noise (i.e., the number of sites that are not successfully assigned to any cluster) is calculated. If the noise is zero, the selected ρ_{cut} is adequate, and the tentative sites are assumed to correspond to the actual crystallographic sites. Otherwise, a higher ρ_{cut} is proposed (e.g., $\rho_{cut}^{new} = \rho_{cut}^{previous} + 0.001$) and the procedure is repeated as depicted in Figure 2.

Once the number and types of sites are established using ρ_{cut} as shown in the bottom panel of Figure 2, the computation of amplitude, occupancy, and the number of neighbors for each site type becomes a straightforward task. Further details of the method and validation are presented in Section S3 of Supporting Information.

In doped systems, the presence of dopants can significantly impact the homogeneity of the density map. This, in turn, complicates the task of finding an appropriate ρ_{cut} to encompass all the crystallographic sites. To overcome this complication, we use the cluster map obtained from the undoped system as our reference and overlay it onto the density map of the doped system for site identification and characterization.

2.5 Estimation of transport properties

The self-diffusion coefficient, D^s, was calculated from the long-time slope of the mean-squared displacement, MSD(t), as[52]:

$$D^s = \lim_{t\to\infty} \frac{d}{dt} \frac{1}{6Nt} \sum_{i=1}^{N} \left\langle \left| r_i(t) - r_i(0) \right|^2 \right\rangle, \quad (3)$$

where N is the number of diffusing atoms and $r_i(t)$ is as defined in Eq. 2. The conductivity, σ, is related to D^s through the Nernst-Einstein equation,

$$\sigma = \frac{c(zF)^2 D^s}{k_B T H_R}, \quad (4)$$

where z and c correspond to the charge and concentration of the charge carriers, respectively. H_R is the Haven ratio, k_B is the Boltzmann constant and F is the Faraday constant[53]. The H_R coefficient measures the correlation between the motion of the ions and is defined as[53,54]

$$H_R = \frac{D^s}{D^\sigma} = \frac{\lim_{t\to\infty} \frac{d}{dt} \sum_{i=1}^{N_{Li}} \left\langle \left| r_i(t) - r_i(0) \right|^2 \right\rangle}{\lim_{t\to\infty} \frac{d}{dt} \sum_{ij=1}^{N} \left\langle [r_i(t) - r_i(0)] \cdot [r_j(t) - r_j(0)] \right\rangle}, \quad (5)$$

where D^σ is the "collective" or "conductivity" diffusion coefficient. If individual ions move preferentially in the same direction, then $H_R < 1$, which is often observed in single ion conductors at high values of c. Under these conditions, ion trajectories are correlated, and the system dynamics deviate from random walk behavior[53]. We have approximated H_R as the ratio of the short-time slopes (approximately the first 6% of the trajectory) of the numerator and denominator, which was shown to offer more reliable statistics[55,56].

3 Results

3.1 $Ga_{0.15}/Sc_y$-LLZO ionic conductivity

It has been observed that Ga^{3+} ions might occupy 24d T_d and 48g/96h O_h sites depending on the sample preparation and/or the sample composition[19,57,58]. In particular, for the case of dual Ga^{3+}/Sc^{3+} doping, Buannic *et al.*[19] demonstrate that Ga^{3+} occupancy of O_h site increases under co-doping with Sc^{3+}. Thus, for

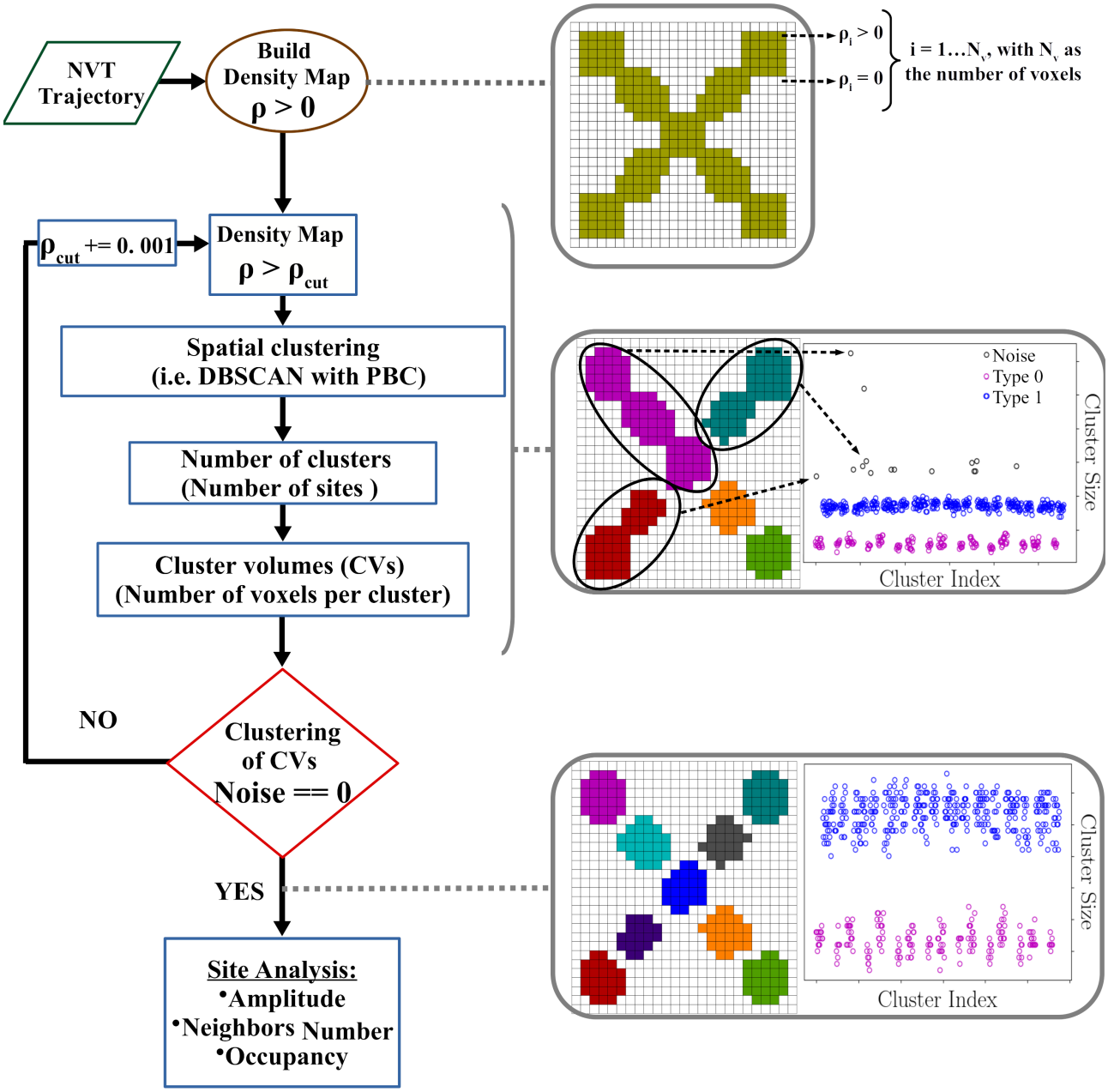

Fig. 2 Outline of the DM-clustering workflow used in this work to characterize the crystallographic sites of diffusive ions. The right-hand schemes depict, from top to bottom: 2D voxel map for voxels with $\rho > 0$, voxels with $\rho > \rho_{cut}$ and non-zero noise, and voxels with $\rho > \rho_{cut}$ and zero noise. Medium and bottom panels include colors for different clusters and cluster size plots, with blue and magenta circles denoting two distinct site types and black circles representing noise.

each Sc^{3+} content, we evaluate multiple distributions of Ga^{3+}, ranging from all Ga^{3+} ions in T_d sites (100%T_d) to all Ga^{3+} ions in O_h sites (0%T_d).

First, we study the extent of unit cell expansion as a function of both the Sc^{3+} content, y, and the distribution of Ga^{3+} ions in the T_d/O_h sites. To this end, we plot the average lattice constant as a function of y in Figure 3 (a). The plot shows good agreement between the calculated and XRD-derived lattice constants (<0.1% difference), highlighting the accuracy of our force field. Likewise, the slight increase in the lattice constant with y is in line with what is expected from substituting Zr^{4+} (ionic radius 0.72 Å[59]) with a larger ion such as Sc^{3+} (ionic radius 0.75 Å[59]). We note that the distribution of Ga^{3+} ions in T_d/O_h sites does not result in any significant alteration of the lattice constant for any given Sc^{3+} content. This finding is consistent with earlier computational and experimental studies[10,57,58].

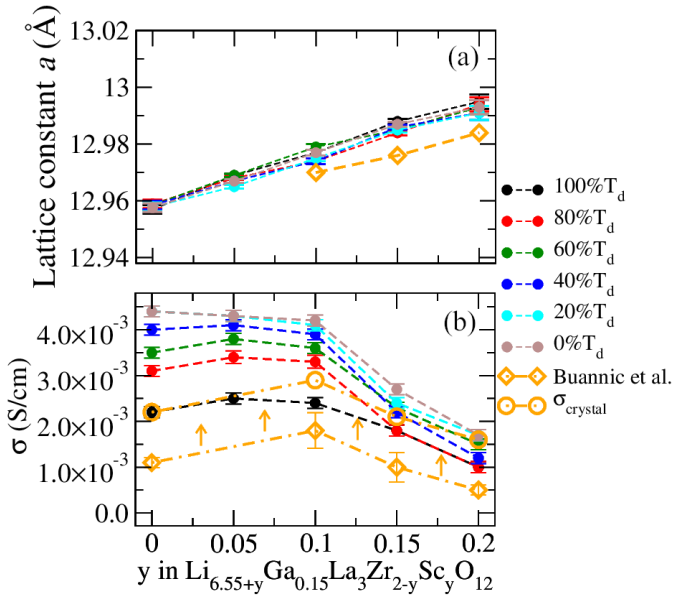

Fig. 3 Calculated lattice constant, a_{cal}, (a) and ionic conductivity, σ_{cal}, (b) of $Ga_{0.15}/Sc_y$-LLZO as functions of Sc^{3+} content (y) for several Ga^{3+} distributions (%T_d) at T = 300 K are denoted with filled circles (error bars correspond to the standard deviation associated with three replicates). Experimental values for a_{exp} and σ_{exp} are included for comparison in (a) and (b) as empty diamonds[19]. The empty circles in (b) represent the values of $\sigma_{crystal}$ as defined in Eq. 6.

A starkly different picture arises when analyzing Li^+ transport. Figure 3 (b) presents the experimental (σ_{exp}, empty diamonds) and calculated (σ_{cal}, filled circles) ionic conductivities for the $Ga_{0.15}/Sc_y$-LLZO system as a function of y, for several Ga^{3+} distributions at 300 K. According to impedance spectroscopy experiments, σ_{exp} increases from 1.1×10^{-3} S/cm for the Sc^{3+}-free sample to an optimal value of 1.8×10^{-3} S/cm at y =0.10. A further increase in y leads to a progressive decrease in σ_{exp}[19]. σ_{cal} overestimates σ_{exp} by an amount that depends on %T_d and y. This can be attributed to the presence of impurities[60] and grain boundaries[61] within the real samples, which are not accounted for in the DFT-based dataset. XRD measurements, on the other hand, can capture the structure of individual crystallites, which is reflected in the accuracy of the predicted lattice constant (Figure 3 (a)).

The calculated conductivities exhibit the following key features:

(i) At $y = 0.0$, σ_{cal} increases as %T_d decreases, with σ_{cal} at 20%T_d nearly double that at 100%T_d. This result lends support to the hypothesis that dopants occupying T_d sites have a more significant disruptive effect on the connectivity of the Li^+ ion network compared to those occupying O_h sites[10–12]. Interestingly, the values of σ_{cal} at 20%T_d and 0%T_d are quite similar, approximately 4.4×10^{-3} S/cm, suggesting that this effect reaches a saturation point.

(ii) The value of σ_{cal} closest to σ_{exp} at $y = 0.0$ corresponds to the 100%T_d case. This finding is consistent with previous experimental reports that have shown Ga^{3+} to preferentially occupy the T_d sites in the absence of other dopants[19,62,63]. Let us define

$$\sigma_{exp} = \sigma_{crystal} - \sigma_{defects} \tag{6}$$

where $\sigma_{crystal}$ is the intracrystalline conductivity and $\sigma_{defects}$ accounts for the effect of defects (e.g., grain boundaries or impurities), and is assumed to be independent of y and %T_d. Thus, taking 100%T_d as the correct Ga^{3+} distribution for y = 0 and equating $\sigma_{crystal}$ to σ_{cal}, we obtain $\sigma_{defects} \sim 10^{-3}$ S/cm. $\sigma_{crystal}$ is shown as the empty circles in Figure 3 (b), and is fully within the range of calculated values of conductivity for all values of y.

(iii) $\sigma_{crystal}$ can be replicated by σ_{cal} for each y_i if we assume the values for %T_d compiled in Table 2. This is in agreement with the suggestion by Buannic *et al.*[19] that the presence of Sc^{3+} increases the proportion of octahedrally coordinated Ga^{3+}, although the precise value for %T_d for each y was not determined in their work.

Table 2 Values of %T_d for different y_i values.

y_i	%T_d
0.00	100
0.05	100
0.10	80
0.15	40
0.20	20

The underlying model in Eq. 6 is analogous to that of a system of parallel resistances, which is most certainly an oversimplification. However, the shape of the theoretical curves in Figure 3 (b) suggests that any additive correction to the experimental conductivities will still produce %T_d values that decrease with y.

To understand the behavior observed in Figure 3 (b) and summarized in items (*i*)-(*iii*) above, we will employ the methodology described in Post-processing Methodology in both the Ga-doped ($Ga_{0.15}/Sc_{0.0}$-LLZO) and Ga/Sc-codoped $Ga_{0.15}/Sc_y$-LLZO) garnet systems.

3.1.1 $Ga_{0.15}/Sc_{0.0}$-LLZO clustering and diffusion analysis

Figure 4 (a) and (b) depicts the clustering based on the average displacement $< d_i >$ (Eq. (2)) and the corresponding MSDs (Eq. (3)) for Li^+ ions within the 100%T_d system at $T = 300$ K. The three subsets identified through the elbow method, Li_1^+, Li_2^+, and Li_3^+, are differentiated by distinct colors. Analogous trends were obtained in relation to the remaining Ga^{3+} distributions (80%T_d to 0%T_d).

The MSDs in Figure 4 (b) reveal that the Li_2^+ (blue line) and Li_3^+ (cyan line) subsets exhibit normal diffusion behavior (i.e., MSD(t) $\sim t$). In contrast, the Li^+ ions in the Li_1^+ subset display subdiffusive behavior (MSD(t) $\sim t^\gamma$ with $\gamma < 1$), which is typically found in confined systems[64]. As a consequence, ions in Li_1^+ are unlikely to significantly contribute to the overall conductivity, and should not be included when estimating σ_{cal} with Eq. (4). In most simulation studies, the calculation of σ involves the consideration of all Li^+ ions, while the influence of inter-ionic correlations is often disregarded by assuming that $H_R = 1$. This approach is generally acceptable, as the influences of both factors tend to counterbalance each other and produce reasonable predictions. Nonetheless, this simplification obscures the mechanisms through which dopants impact ionic conduction, which is precisely the scope of this article.

For simplicity, we will merge the high-mobility Li^+ ions in subsets Li_2^+ and Li_3^+ into a new subset denoted Li_{hm}^+. Likewise, the low-mobility Li^+ ions in subset Li_1^+ will be referred to as Li_{lm}^+. Thus, our estimation of D^s and H_R exclusively considers the ions within the Li_{hm}^+ subset. An effective charge carrier concentration, c^{eff}, corresponding to that of the Li_{hm}^+ subset should, be concomitantly employed in Eq. (4) as opposed to the total Li^+ ion concentration. When all Li^+ ions are considered, and H_R is taken as unity, σ_{cal} follows a rather different behavior to that shown in Figure 3 (b) (see Figure S7 in the Supporting Information). Recent experiments by Nozaki *et al.*[29] on Nb-doped LLZO underscore the significance of c^{eff} in the ionic conductivity, suggesting that as little as $\sim$ 10-15% of the Li^+ ions in this system act as effective charge carriers.

The three factors determining σ_{cal} in Eq. (4), namely c^{eff}/c, D^s, and H_R, are depicted as a function of %T_d for $Ga_{0.15}/Sc_{0.0}$-LLZO in Figure 5. Here c^{eff}/c is the proportion of Li^+ ions effectively contributing to the ionic conductivity and c is the total Li^+ concentration. As shown in Figure 5, c^{eff}/c ranges between $\sim$ 46% and 56% of the total number of charge carriers, and thus, nearly half of all available Li^+ ions are essentially trapped in the sense that their diffusion paths do not span the entire length of the simulation box. Moreover, c^{eff}/c decreases by $\sim$ 18% as the amount of Ga^{3+} ions in T_d sites increases from 0% to 100%, indicating that ion trapping is mildly impacted by the distribution of dopant within the Li^+ sublattice. A similar trend is observed for D^s, which decreases by 34% between 0%T_d and 100%T_d.

$H_R \leq 1$ (Eq. (5)) is a measure of the degree of correlation in the motion of ions, with $H_R = 1$ indicating ideal uncorrelated diffusion. The H_R values in Figure 5 agree well with those reported by Morgan[65] in his lattice-gas Monte Carlo simulations of cubic LLZO with different Li^+ contents. For a Li^+ content of 6.55, his H_R values ranged from 0.3 to 0.5. Interestingly, Figure 5 reveals a subtle upward trend in H_R as %T_d increases, suggesting that increasing the quantity of Ga^{3+} ions in T_d sites is somewhat detrimental to collective Li^+ ion diffusion.

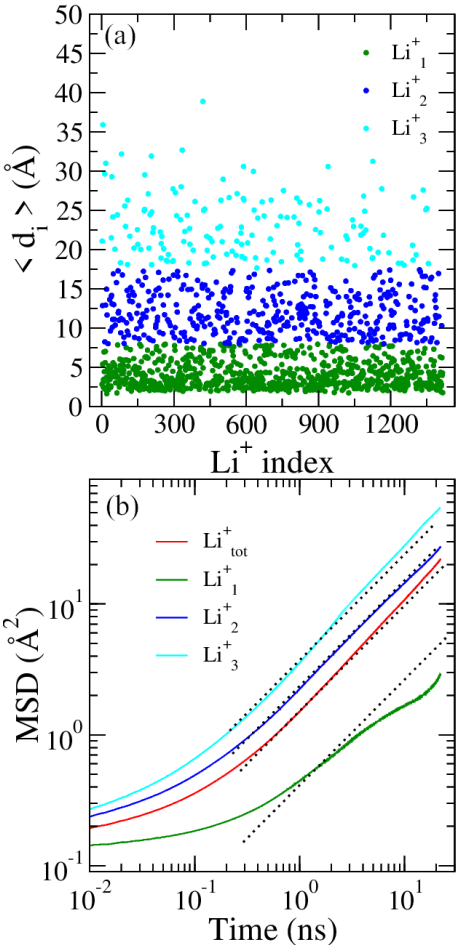

Fig. 4 Average displacement $< d_i >$ (a) and MSDs(t) (b) for Li^+ ions in the $Ga_{0.15}/Sc_{0.0}$-LLZO system at 100%T_d and T = 300 K. The different subsets of Li^+ ions (Li_1^+, Li_2^+, and Li_3^+) are represented by green, blue, and cyan dots (a) and solid lines (b), respectively, while the solid red line in (b) denotes the total MSDs for all Li^+ ions ($Li_{tot}^+ = Li_1^+ + Li_2^+ + Li_3^+$). Black dotted lines are obtained by the linear fitting in the log-log scale identifying the diffusive regime (MSD $\sim t$).

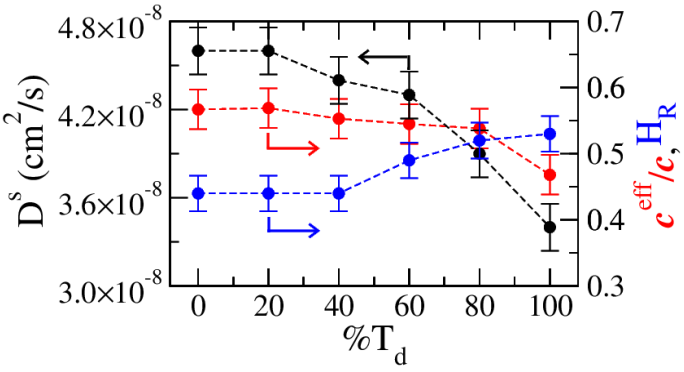

Fig. 5 Calculated self diffusivity D^s (black dots left-axis), relative effective concentration c^{eff}/c (red dots right-axis) and Haven ratio, H_R (blue dots right-axis) for $Ga_{0.15}/Sc_{0.0}$-LLZO as a function of $\%T_d$ (error bars correspond to the standard deviation associated with three replicates).

From the discussion above, it is clear that the distribution of Ga^{3+} ions has a mild to moderate impact on the variables controlling the conductivity (D^s, H_R and c^{eff}), and always results in a decrease in σ as $\%T_d$ increases. While single Ga^{3+} ion doping tends to stabilize the $100\%T_d$ structure[63], tuning of the Ga^{3+} ion distribution can be achieved through co-doping, as we shall discuss later. First, we will address why c^{eff}/c is so strongly diminished by the presence of Ga^{3+} ions.

3.1.2 $Ga_{0.15}/Sc_{0.0}$-LLZO occupancy analysis

The investigation of Li-site occupancy has been undertaken both experimentally and theoretically in doped and undoped garnet materials[30,31,34,66–68]. In this study, we have employed the methodology described in Figure 2 to calculate the occupancy of the Li^+ sites in the simulated systems.

The calculated occupancies for $Ga_{0.15}/Sc_{0.0}$-LLZO are presented as a function of $\%T_d$ in Figure 6. For comparison, we have included the experimental occupancies for Ta-doped LLZO with a similar Li content ($\sim$ 6.5 mol)[30,66,67]. Importantly, the variable $\%T_d$ cannot be used for Ta-doping, since Ta^{4+} substitutes Zr^{3+} in LLZO. The occupancies predicted through our clustering approach, combined with the newly developed force field, match remarkably well the Li-site occupancies in Ta-doped LLZO. The small differences with experimental results[30,66,67] can be attributed to slight discrepancies in the Li molar contents and the specific dopant used in the experiments (Ta) and our simulation (Ga).

Figure 6 also shows the average occupancies in the surroundings of the Ga^{3+} ions (within a radius of 3.3 Å) in blue. While the calculated occupancies of T_d and O_h sites are nearly constant, the average occupancies near Ga^{3+} ions decrease significantly as $\%T_d$ increases. Previous work demonstrated that Ga^{3+}/Al^{3+} dopants tend to trap vacancies in their surroundings, leaving their first nearest neighbor (1NN) shell in the Li-ion lattice largely unoccupied[28]. Since Ga^{3+} ions in T_d positions have four 1NN Li^+ sites (Figure 6(c)) and those in O_h positions have only two (Figure 6 (b)), the average occupancy in the vicinity of the Ga^{3+} ion must naturally decrease as $\%T_d$ increases. Below, we demonstrate that these permanent vacancies stabilize low-mobility Li^+ ions at 2NN and even 3NN positions.

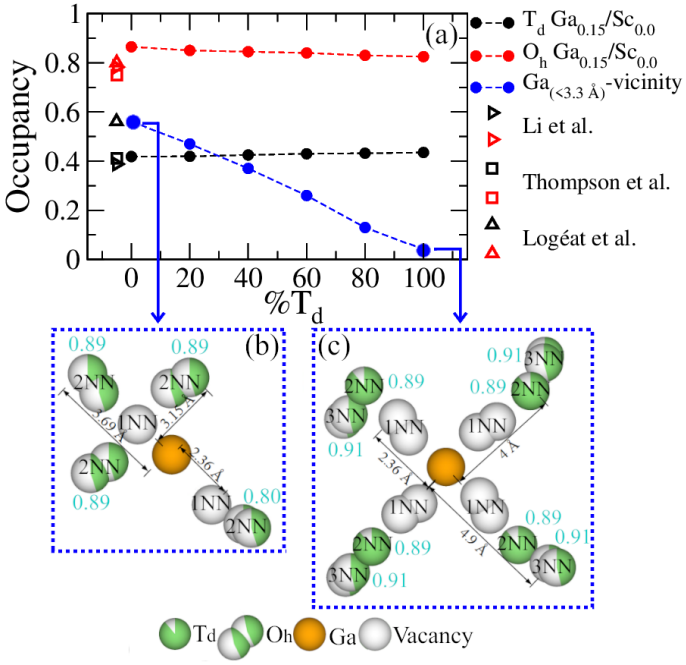

Fig. 6 Li-site occupancy of $Ga_{0.15}/Sc_{0.0}$-LLZO as a function of the Ga distribution $\%T_d$ at 300 K (a). The black and red dots represent the occupancy of T_d and O_h sites, respectively, while $\%T_d$ refers exclusively to the Ga^{3+} ions. The average occupancy of the sites neighboring Ga^{3+} ions (within 3.3 Å) is depicted as blue dots (a). To provide a comparative analysis, experimental values for Ta-doped LLZO with Li content 6.5 mol are included as empty symbols[30,66,67]. In the bottom panels (b) and (c), schematic depictions illustrate the coordination shells of Ga^{3+} ions in both $0\%T_d$ and $100\%T_d$ systems. Additionally, these depictions include the identification of the first, second, and third nearest neighbor Li^+ sites, denoted as 1NN, 2NN, and 3NN, respectively. Values in cyan denote the average occupancy of the site. The crystallographic inter-site distances are also shown.

Figure 7 displays the average Li-site occupancies as a function of the distance r from Ga^{3+} ions for the distinct Li subsets Li_{hm} and Li_{lm}, in the $0\%T_d$ and $100\%T_d$ systems. We will refer to this variable as the radial occupancy, $rocc(r)$. At a given r^*, adding $rocc(r^*)$ for Li_{hm} and Li_{lm} yields the total Li-site occupancy at $r = r^*$. The method to extract $rocc(r)$ departing from the site identification approach described in Figure 2 is outlined in Section 3 of the Supporting Information. Notice that $rocc(r)$ is qualitatively similar to the radial distribution function, $g(r)$, as it indirectly measures the average Li^+ ion density with respect to a central Ga^{3+} ion. However, $rocc(r)$ can readily provide such information for each identified site type without prior crystallographic knowledge.

Let us consider first the evolution of $rocc(r)$ with r in the $0\%T_d$ system, depicted in Figure 7 (a). The value of $rocc(r)$ up to the 2NN shell of an octahedrally coordinated Ga^{3+} ion, $rocc(r < 4$ Å$)$, is significantly larger for Li_{lm} than for Li_{hm} in the O_h sites, with the former subset accounting for 82% of the total site occupancy. Referring to the schematic representation in Figure 6 (b), this means that the 2NN sites are primarily occupied by low-mobility Li^+ ions, for which the average displacement over the course of a simulation run is far below the simulation box length

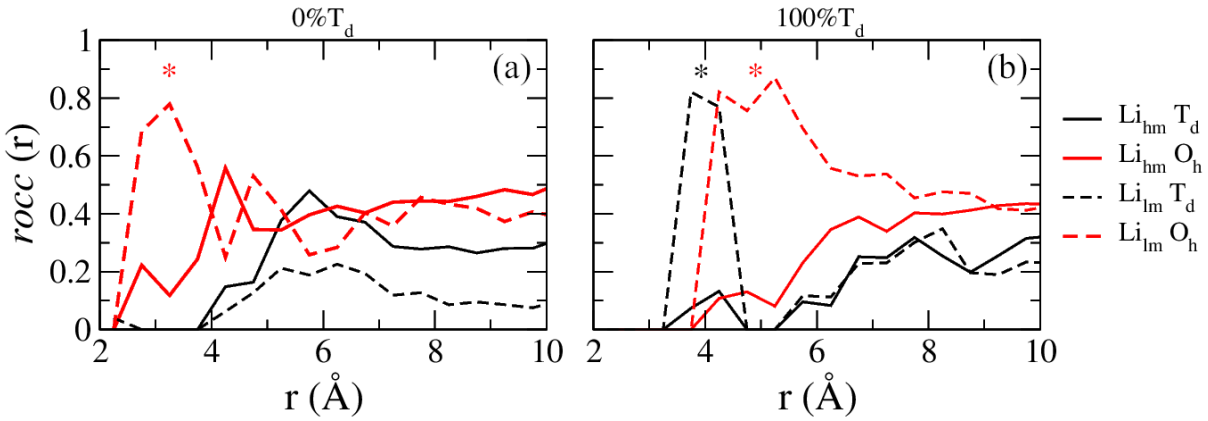

Fig. 7 Radial occupancy, $rocc(r)$, of Li^+ sites around Ga^{3+} in $Ga_{0.15}/Sc_{0.0}$-LLZO for two Li subsets, Li_{hm} (solid line) and Li_{lm} (dashed line). The two extreme Ga distributions (a) 0%T_d and (b) 100%T_d were analysed. The black and red colors denote the occupancy of T_d and O_d sites, respectively. The asterisks represent the distances to the occupied Li^+ sites illustrated in Figure 6 (b) and (c), respectively.

(see Figure 4 (a)): they are effectively trapped. Beyond this point ($r > 4$ Å), the occupancy of the O_h sites stabilizes, showing equal proportions of Li_{lm} and Li_{hm} ions. Interestingly, the Td sites are preferentially occupied by ions from the Li_{hm} subset rather than the Li_{lm} subset.

For the 100%T_d system (Figure 7 (b)), Li^+ ions in the Li_{lm} subset are predominant up to $r \approx 4.5$ Å (for T_d sites) and $r \approx 7$ Å (for O_h sites). These correspond, respectively, to the 2NN and 3NN positions represented in Figure 6 (c). The XRD-based crystallographic locations[6] of these sites in pristine LLZO are indicated with asterisks in Figure 7 (b). As expected, the distorting effect of the dopants and thermal vibrations generate the spread on the peaks observed in the curves (which is also typical in $g(r)$ curves). The total radial occupancy for each site type around r^* is higher than the average site occupancy in $Ga_{0.15}/Sc_{0.0}$-LLZO (Figure 6 (a)), which is ~ 0.42 for T_d and ~ 0.84 for O_h sites.

The above suggests that Ga^{3+} ions doped in T_d sites not only trap Li^+ vacancies in the 1NN O_h sites (Figure 6 (c)) but also hamper the mobility of Li^+ ions within an approximate range of 7 Å, as reflected in the high occupancy values for Li_{lm} in the 2NN and 3NN positions (Figure 7 (b)). In contrast, high Li_{lm} occupancy only reaches the 2NN at $r \approx 4$ Å for the Ga^{3+} ions doped in O_h sites, explaining the progressive reduction in D^s with 100%T_d depicted in Figure 5.

Figures 8 (a) and (b) display the density maps of Li_{hm} ions for the 0%T_d and 100%T_d systems, respectively. These maps offer a clear visualization of the long-range diffusion paths within the crystal structure. An examination of the number of sites visited by Li_{hm} ions indicates that the Li^+ ion pathways in the 0%T_d and 100%T_d systems encompass 70% and 50% of the total number of Li^+ sites, respectively. Thus, increasing the fraction of Ga^{3+} ions in O_h sites results in a moderate extension of the conductive network.

So far, we have found that the distribution of Ga^{3+} ions has a profound impact on the occupancy of the surrounding Li^+ sites, giving rise to discrete islands that do not participate in the diffusion process. The number of sites within these islands increases as %T_d increases, consequently leading to a reduction in effective charge carrier concentration and diffusivity. Furthermore, as %T_d increases, there is an observed increase in H_R (Figure 5), which suggests that collective Li^+ ion diffusion deteriorates. This may be due, at least partially, to the circular trajectories followed by Li^+ ions as they diffuse around these islands, which results in a slight reduction in the overall center-of-mass displacement for collections of locally correlated Li^+ ions.

In the following section, we will delve into Sc-doping as a strategy to tune the site distribution of Ga^{3+} ions. We will demonstrate how our force field, in conjunction with our DM-clustering methodology, can explain the variation of the conductivity (σ) with the parameter y, as depicted in Figure 3 (b).

3.1.3 $Ga_{0.15}/Sc_y$-LLZO diffusion analysis

Now that the effect of the distribution of Ga^{3+} ions on the effective charge carrier concentration, diffusivity, and Li^+ site occupancy has been described, we address the impact of Sc content in $Ga_{0.15}/Sc_y$-LLZO. To this end, we assume the Ga^{3+} ion distributions presented in Table 2, which were adjusted to match the experimental conductivities reported by Buannic et al.[19] following the model presented in Eq. 6.

While Table 2 reports a progressive decrease in %T_d with y, which following the discussion above should lead to a concomitant increase in conductivity, the experimental data shows that σ displays a maximum at $y = 0.1$. To understand the origin of this discrepancy, Figure 9 displays the specific factors influencing ionic conductivity, which includes D^s, c^{eff} (normalized by $c(y=0)$), and H_R, all plotted against y.

D^s and c^{eff} exhibit points of maxima at $y = 0.10$, while H_R displays a minimum at this Sc content. While the variations in these three variables are small, their combined contribution produces the relatively large maximum in σ^{exp} observed in Figure 3 at $y = 0.10$. In particular, the behavior of D^s and c^{eff} is starkly different from that depicted in Figure 5 for a constant Ga content in Sc-free LLZO, which shows that decreasing %T_d (as expected with increasing y) leads to a monotonic increase in these variables. Therefore, the presence of a maximum in σ^{exp} must be associated with (i) the local effect of Sc^{3+} ions on the Li^+ ion mo-

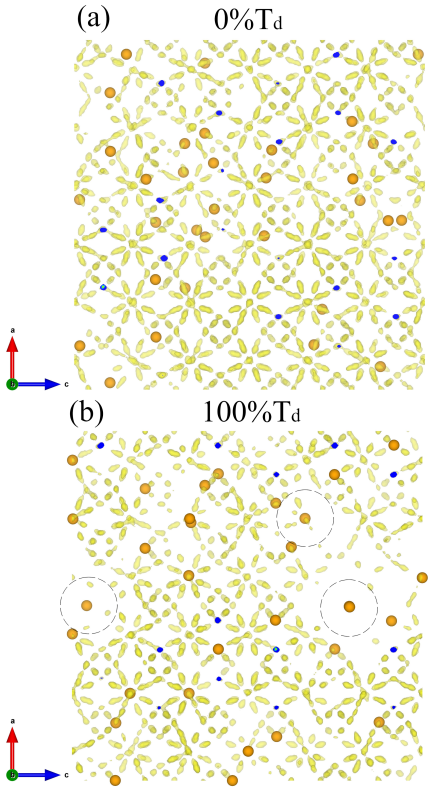

Fig. 8 Density maps of Li_{hm} ions in the (010) plane for $Ga_{0.15}/Sc_{0.0}$-LLZO with 0%T_d (a) and 100%T_d (b) at 300K. The remaining orientations (100) and (001) are included in Section S6 of the Supporting Information. Ga^{3+} ions are represented as orange spheres. Dashed circles highlight areas around Ga^{3+} atoms that were not visited by Li^+ ions during the simulated trajectory.

bility and/or (*ii*) the increase in Li^+ molar content arising from Sc doping. We evaluate these two possibilities below.

3.1.4 $Ga_{0.15}/Sc_y$-LLZO occupancy analysis

For undoped LLZO, the Li-site occupancies are physically limited to $0.333 \leq T_d \leq 0.55$ and $0.88 \leq O_h \leq 1.0$[69]. These limits change for doped systems and depend on the Li^+ concentration, the host site, and the dopant type[70]. For $Ga_{0.15}/Sc_y$-LLZO, we have derived them as a function of y in Section S5 of the Supporting Information. The allowed occupancies are illustrated in Figure 10 (a) as the gray (for O_h sites) and red (T_d sites) shaded areas.

The Li-site occupancies for T_d and O_h sites in the simulated $Ga_{0.15}/Sc_y$-LLZO systems are depicted in Figure 10 (a) as black and red dots, respectively. Both site types exhibit occupancy values that fall well within the established limits, underscoring the precision of our force field and site identification approach. Multi-doped systems can be highly locally distorted, and the trapping of vacancies may make site occupancy estimations difficult without prior detailed knowledge of the system's crystallography. Here, MD trajectories are the only required input. Experimentally determined occupancies for X-doped LLZO systems (X = Ta and Sb) are included as empty symbols at their corresponding Li-molar concentrations. For the O_h sites, the experimental and predicted occupancies match closely. T_d site occupancies tend to display a more pronounced divergence, especially at a Li-molar content of

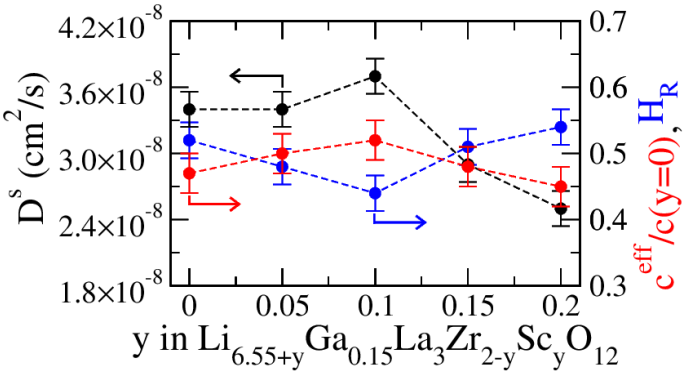

Fig. 9 Calculated self diffusivity D^s (black dots left-axis), (reduced) effective concentration $c^{\text{eff}}/c(y=0)$ (red dots right-axis) and Haven ratio, H_R (blue dots right-axis) of $Ga_{0.15}/Sc_y$-LLZO as a function of the Sc content y, following the %$T_d(y)$ values presented in Table 2 (error bars correspond to the standard deviation associated with three replicates).

6.7. This may be partly attributed to the challenges associated with producing cubic LLZO at high Li-molar contents using small quantities of a single dopant. In such cases, there is a significant probability of obtaining a mixture of both tetragonal and cubic phases[28,71].

Interestingly, despite the increase in Li^+ ion content induced by the addition of Sc^{3+} ions (one Li^+ per Sc^{3+}), we observe no discernible alterations in the occupancy of the T_d sites. In contrast, at the O_h sites, there is a modest but noteworthy increase in occupancy with y. That is, the Li^+ ions added to the system through Sc-doping tend to preferentially occupy O_h sites.

The average occupancy in the vicinity of the Sc^{3+} ions (within 4.2 Å) is represented by blue dots in Figure 10 (a). It remains almost constant around the median of the global occupancies of the two types of Li^+ sites. Figure 10 (b) presents a schematic representation of the Li-site coordination shell for Sc^{3+} ions, with the corresponding occupancy values for the six 1NN O_h and 2NN T_d sites. Both the 1NN O_h and 2NN T_d sites exhibit occupancies (0.85 and 0.45, respectively) that closely match the global values associated with their corresponding site types. Notably, these values remain consistent across all Sc contents, supporting the claim that Sc-doping does not exert a substantial effect on the crystalline structure, as indicated in Figure 3 (a).

The occupancies associated with the Li subsets Li_{hm} and Li_{lm} are also included in Figure 10 (b) with the labels -hm and -lm. For 2NN T_d sites, both low and high-mobility Li^+ ions exhibit similar occupancy values (0.21 for -hm and 0.24 for -lm). This observation indicates that there is no discernible effect of Sc-doping on the mobility of Li^+ ions at these sites. In contrast, when examining the 1NN O_h sites, we observe distinct occupancy values for Li_{hm} and Li_{lm}: 0.31 and 0.54, respectively, suggesting that Sc^+ ions reduce the mobility of Li^+ ions within its 1NN Li-site shell. This can be attributed to the fact that the substitution of Sc^{3+} into the Zr^{4+} sites leads to a reduction in the site charge, thereby reducing the Coulombic repulsion between Sc^{3+} and Li^+ ions in 1NN O_h sites. Therefore, reduced mobility areas around Sc^{3+} ions form as y increases, but the range of this effect is limited.

On the other hand, increasing the Sc^{3+} content increases the

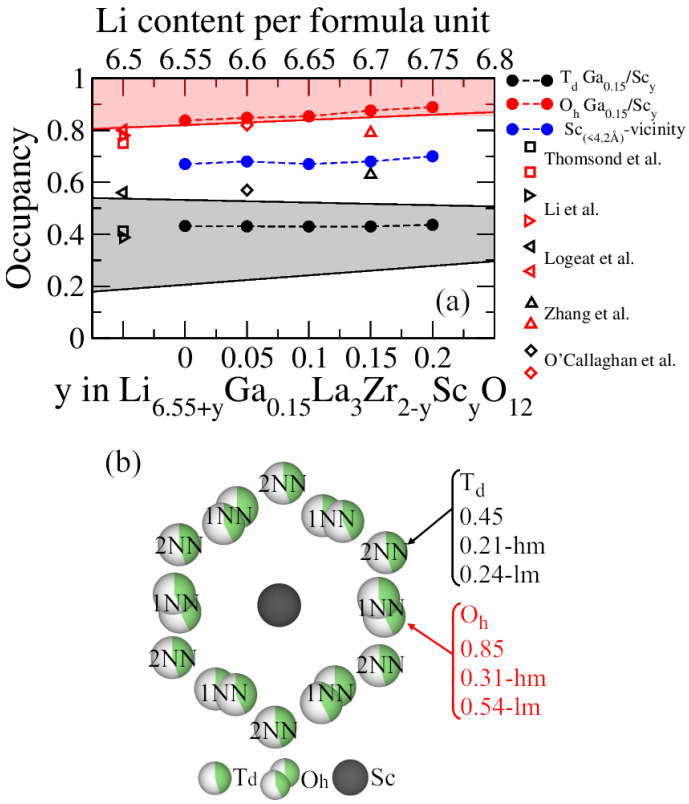

Fig. 10 Li-site occupancy of $Ga_{0.15}/Sc_y$-LLZO as a function of the Sc^{3+} content y, at 300 K (a). Black and red dots denote T_d and O_h sites, respectively. Average occupancy near Sc^{3+} ions (< 4.2 Å) is denoted by blue dots. The permitted occupancy ranges for the two types of sites are represented by black and red shaded areas, respectively. Experimental occupancies for X-doped LLZO systems (with X = Ta and Sb) with Li-molar contents close to those evaluated in this study are included as empty symbols[30,67,68,72,73]. In the bottom panel (b), a schematic depiction illustrates the Li-site coordination shell of Sc^{3+} ions. The occupancy values of the T_d and O_h sites are included in black and red, respectively. Meanwhile, the values corresponding to the Li subsets, Li_{hm} and Li_{lm}, are denoted with the label -hm and -lm.

Li-molar concentration and reduces the number of available vacancies. To gain a deeper insight into how reducing lithium vacancies affects D^s, we have calculated the average inter-site jump frequency, k, as follows:

$$k = \frac{< d_{tr} >}{< d_s > t}, \tag{7}$$

where

$$< d_{tr} >= \frac{1}{N} \sum_{i=1}^{N} \sum_{j=1}^{n} |r_i((j+1)\Delta t) - r_i(j\Delta t)|, \tag{8}$$

with n, N and Δt as defined in Eq. 2 and Eq.3, respectively. Specifically, $< d_{tr} >$ denotes the average distance traveled by Li_{hm} ions (adding all the absolute displacements), while $< d_s >$ is the average distance between adjacent T_d and O_h sites (~2.5 Å), and t is the simulation time. Note that subdiffusive Li_{lm} ions are not accounted for, as they were not considered in the calculation of D^s. Figure 11 shows the behavior of k against y. Clearly, k decreases with increasing Sc^{3+} content, with a steeper drop below $y = 0.10$.

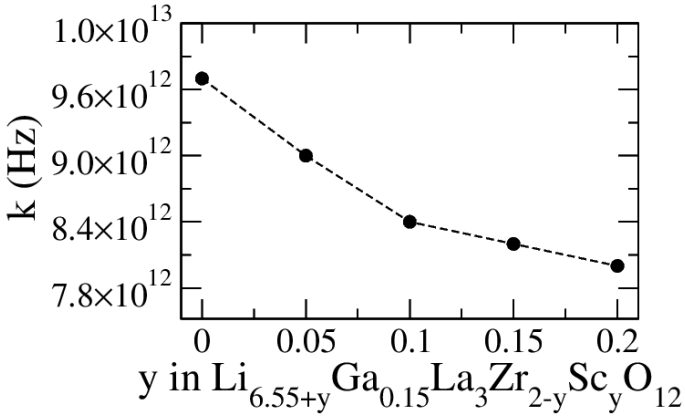

Fig. 11 Jump frequency, k, of Li_{hm} ions for $Ga_{0.15}/Sc_y$-LLZO as a function of the Sc content y, following the $\%T_d(y)$ values presented in Table 2.

With these elements at hand, we can now explain the maximum D^s that was observed in Figure 9. There are two competing mechanisms coming into play here. On the one hand, the increase in the amount of Ga^{3+} ions in O_h sites tends to boost D^s. On the other hand, the decrease in the number of vacancies has a detrimental effect on the jump frequency, leading to a reduction in D^s. The former mechanism prevails for $y < 0.10$, while the second one dominates for $y > 0.10$. Likewise, for H_R, the presence of Ga^{3+} ions in O_h sites tends to increase collective Li^+ ion diffusion (i.e., reducing H_R), while the lower vacancy content causes the Li^+ ions to retrace their path more often, diminishing collective displacement and consequently increasing H_R. The combined effect of these two variables (and to a lesser extent that of c^{eff}, which displays milder variations as shown in Figure 9), generates the behavior reported for the experimental conductivity[19] depicted in Figure 3.

4 Conclusions

In this work, we have introduced and applied a DM-clustering method along with an in-house, material-specific force field combined with our advanced sampling techniques to investigate the dynamics of Li^+ ions in dual-doped $Ga_{0.15}/Sc_y$-LLZO. The proposed DM-based approach can be easily adapted to the analysis of MD trajectories for other solid electrolytes, allowing the identification of site occupancies, active diffusion paths, and high-mobility charge carriers that effectively contribute to ionic conduction. The impact of multi-doping strategies on these variables can then be systematically addressed from a theoretical viewpoint following the framework presented in this work.

By initially analyzing Sc^{3+}-free, $Ga_{0.15}/Sc_0$-LLZO, we found that it is possible to enhance the ionic conductivity (σ) by increasing the proportion of Ga^{3+} ions occupying octahedral (O_h) Li^+ sites, in contrast to the thermodynamically favored tetrahedral (T_d) Li^+ sites typically preferred in single Ga-doping scenarios[11,12]. A comprehensive analysis of Li-site occupancy, conducted through our DM-clustering methodology, revealed the structural underpinnings of this observation. Ga^{3+} ions located

in T_d sites have been shown to reduce the mobility of Li^+ ions in both the 2NN T_d and 3NN O_h sites, aligning with earlier findings based on radial distribution function analysis[27]. In contrast, Ga^{3+} ions in O_h sites only have a detrimental impact on ionic mobility up to the 2NN O_h sites.

Previous DFT simulations showed that co-doping with Sc^{3+} at the Zr^{4+} site promotes the formation of octahedrally coordinated Ga^{3+} ions[19], thus reducing the proportion of Ga^{3+} in T_d sites ($\%T_d$). By combining atomistic simulations of $Ga_{0.15}/Sc_y$-LLZO ($0 < y \leq 0.20$) with available experimental data[19], we verified that $\%T_d$ is likely to decrease with increasing Sc^{3+} content, and provided predictions for $\%T_d$ as a function of y. Notably, decreasing $\%T_d$ through the incorporation of Sc^{3+} ions does not lead to a monotonic increase in σ (which was found to be the case for single Ga-doping at the corresponding $\%T_d$ values), but leads to a maximum at $y = 0.10$.

We found that the Sc^{3+} ions do not considerably influence the mobility of Li^+ ions in their immediate vicinity. However, adding Sc^{3+} increases the Li-molar content and reduces the number of vacancies in active diffusion paths. This produces a reduction in the inter-site jumping frequency, k, negatively impacting the diffusivity, D^s. The competing effects on σ of a decreasing $\%T_d$ and a decreasing k lead to the observed maximum in conductivity. We stress that σ is not only a function of D^s, but also depends on the effective concentration of charge carriers (c^{eff}) and the Haven ratio (H_R). Nonetheless, D^s was found to be the variable most considerably impacted by y in this particular system.

Finally, this work shows that substitutional doping in the O_h sites of cubic LLZO remains a viable strategy for enhancing ionic conductivity. Moreover, co-doping strategies promoting Ga^{3+} ion occupation of O_h sites without the concomitant loss of active vacancies may be a promising avenue to further increase the performance of LLZO-based solid electrolytes.

Author Contributions

The manuscript includes simulations performed by H. A. C. (Sections 2) and methodology developed by H. A. C., M. R. B., and E. A. (Sections 2 and 3). Formal analysis was carried out by H. A. C., M. R. B., and E. A. The manuscript was primarily written by H. A. C., M. R. B. and E. A with additions contributions from H. F., T v. M. and J. C., who provided conceptualization and supervision of the work. Reviewing and editing were performed by all the authors.

Conflicts of interest

There are no conflicts to declare.

Acknowledgements

We acknowledge financial support by the Ministerio de Economía y Competitividad (MICINN) of the Spanish Government through BCAM Severo Ochoa accreditation CEX2021-001142-S, PID2019-104927GB-C22, PID2022-136585NB-C22 grants and "PLAN COMPLEMENTARIO MATERIALES AVANZADOS 2022-2025", PROYECTO N°:1101288 [ELKARTEK ICME]. This work was supported by the BERC 2022-2025 Program, by ELKARTEK Programme, grants KK-2022/00006, KK-2023/00017 and by IKUR Programme funded by the Basque Government. This work has been possible thanks to the computing infrastructure of the i2BASQUE academic network, DIPC Computer Center, RES BSC (QHS-2022-3-0027), and the technical and human support provided by IZO-SGI SGIker of UPV/EHU. The work has been performed under the Project HPC-EUROPA3 (INFRAIA-2016-1-730897), with the support of the EC Research Innovation Action under the H2020 Programme; in particular, H. A. C. gratefully acknowledges the support of the School of Chemistry, University of St. Andrews, and the computer resources (ARCHER2) and technical support provided by EPCC.

Notes and references

1 S. G. Booth, A. J. Nedoma, N. N. Anthonisamy, P. J. Baker, R. Boston, H. Bronstein, S. J. Clarke, E. J. Cussen, V. Daramalla, M. D. Volder, S. E. Dutton, V. Falkowski, N. A. Fleck, H. S. Geddes, N. Gollapally, A. L. Goodwin, J. M. Griffin, A. R. Haworth, M. A. Hayward, S. Hull, B. J. Inkson, B. J. Johnston, Z. Lu, J. L. MacManus-Driscoll, X. M. D. I. Labalde, I. McClelland, K. McCombie, B. Murdock, D. Nayak, S. Park, G. E. Pérez, C. J. Pickard, L. F. J. Piper, H. Y. Playford, S. Price, D. O. Scanlon, J. C. Stallard, N. Tapia-Ruiz, A. R. West, L. Wheatcroft, M. Wilson, L. Zhang, X. Zhi, B. Zhu and S. A. Cussen, *APL Materials*, 2021, **9**, 109201.

2 Y. Yan, J. Ju, S. Dong, Y. Wang, L. Huang, L. Cui, F. Jiang, Q. Wang, Y. Zhang and G. Cui, *Advanced Science*, 2021, **8**, 2003887.

3 Q. Zhao, S. Stalin, C.-Z. Zhao and L. A. Archer, *Nat Rev Mater*, 2020, **5**, 229–252.

4 Y. Wang, H. Qu, B. Liu, X. Li, J. Ju, J. Li, S. Zhang, J. Ma, C. Li, Z. Hu, C.-K. Chang, H.-S. Sheu, L. Cui, F. Jiang, E. R. H. van Eck, A. P. M. Kentgens, G. Cui and L. Chen, *Nat Commun*, 2023, **14**, 669.

5 Y. Zheng, Y. Yao, J. Ou, M. Li, D. Luo, H. Dou, Z. Li, K. Amine, A. Yu and Z. Chen, *Chem. Soc. Rev.*, 2020, **49**, 8790–8839.

6 J. Awaka, N. Kijima, H. Hayakawa and J. Akimoto, *J. Solid State Chem.*, 2009, **182**, 2046–2052.

7 C. A. Geiger, E. Alekseev, B. Lazic, M. Fisch, T. Armbruster, R. Langner, M. Fechtelkord, N. Kim, T. Pettke and W. Weppner, *Inorganic Chemistry*, 2011, **50**, 1089–1097.

8 J. Awaka, A. Takashima, K. Kataoka, N. Kijima, Y. Idemoto and J. Akimoto, *Chem. Lett.*, 2011, **40**, 60–62.

9 R. Jalem, Y. Yamamoto, H. Shiiba, M. Nakayama, H. Munakata, T. Kasuga and K. Kanamura, *Chemistry of Materials*, 2013, **25**, 425–430.

10 R. Jalem, M. Rushton, W. Manalastas, M. Nakayama, T. Kasuga, J. A. Kilner and R. W. Grimes, *Chem. Mater.*, 2015, **27**, 2821–2831.

11 D. O. Shin, K. Oh, K. M. Kim, K.-Y. Park, B. Lee, Y.-G. Lee and K. Kang, *Sci. Rep.*, 2015, **5**, 18053.

12 A. Kim, J.-H. Kang, K. Song and B. Kang, *ACS Appl. Mater. Interfaces*, 2022, **14**, 12331–12339.

13 D. Rettenwander, G. Redhammer, F. Preishuber-Pflugl, L. Cheng, L. Miara, R. Wagner, A. Welzl, E. Suard, M. M. Doeff, M. Wilkening, J. Fleig and G. Amthauer, *Chemistry of Materi-*

als, 2016, **28**, 2384–2392.

14 C. Bernuy-López, W. Manalastas, J. M. López del Amo, A. Aguadero, F. Aguesse and J. A. Kilner, *Chemistry of Materials*, 2014, **26**, 3610–3617.

15 J.-F. Wu, E.-Y. Chen, Y. Yu, L. Liu, Y. Wu, W. K. Pang, V. K. Peterson and X. Guo, *ACS Appl. Mater. Interfaces*, 2017, **9**, 1542–1552.

16 Y. Zhou, X. Li, Y. Yang, X. Huang and B. Tian, *ACS Appl. Energy Mater.*, 2022, **5**, 13817–13828.

17 D. K. Schwanz, A. Villa, M. Balasubramanian, B. Helfrecht and E. E. Marinero, *AIP Advances*, 2020, **10**, 035204.

18 V. Thangadurai and W. Weppner, *J American Ceramic Society*, 2005, **88**, 411–418.

19 L. Buannic, B. Orayech, J.-M. López Del Amo, J. Carrasco, N. A. Katcho, F. Aguesse, W. Manalastas, W. Zhang, J. Kilner and A. Llordés, *Chemistry of Materials*, 2017, **29**, 1769–1778.

20 J.-F. Wu, W. K. Pang, V. K. Peterson, L. Wei and X. Guo, *ACS Appl. Mater. Interfaces*, 2017, **9**, 12461–12468.

21 L. Shen, L. Wang, Z. Wang, C. Jin, L. Peng, X. Pan, J. Sun and R. Yang, *Solid State Ionics*, 2019, **339**, 114992.

22 Y. Meesala, Y.-K. Liao, A. Jena, N.-H. Yang, W. K. Pang, S.-F. Hu, H. Chang, C.-E. Liu, S.-C. Liao, J.-M. Chen, X. Guo and R.-S. Liu, *J. Mater. Chem. A*, 2019, **7**, 8589–8601.

23 L. H. Abrha, T. T. Hagos, Y. Nikodimos, H. K. Bezabh, G. B. Berhe, T. M. Hagos, C.-J. Huang, W. A. Tegegne, S.-K. Jiang, H. H. Weldeyohannes, S.-H. Wu, W.-N. Su and B. J. Hwang, *ACS Appl. Mater. Interfaces*, 2020, **12**, 25709–25717.

24 M.-Y. Kim, B.-S. Kang, Y.-W. Song, S.-J. Park, J. Lim, H. Kim, Y. Hong, H.-S. Kim and J.-H. Han, *J. Electrochem. Soc.*, 2022, **169**, 120506.

25 X. Zhou, L. Huang, O. Elkedim, Y. Xie, Y. Luo, Q. Chen, Y. Zhang and Y. Chen, *J. Alloys Compd.*, 2022, **891**, 161906.

26 Y. Tian, Y. Zhou, W. Wang and Y. Zhou, *Ceramics International*, 2022, **48**, 963–970.

27 F. A. García Daza, M. R. Bonilla, A. Llordés, J. Carrasco and E. Akhmatskaya, *ACS Appl. Mater. Interfaces*, 2019, **11**, 753–765.

28 M. R. Bonilla, F. A. García Daza, J. Carrasco and E. Akhmatskaya, *Acta Mater.*, 2019, **175**, 426 – 435.

29 H. Nozaki, M. Harada, S. Ohta, I. Watanabe, Y. Miyake, Y. Ikedo, N. H. Jalarvo, E. Mamontov and J. Sugiyama, *Solid State Ionics*, 2014, **262**, 585–588.

30 T. Thompson, A. Sharafi, M. D. Johannes, A. Huq, J. L. Allen, J. Wolfenstine and J. Sakamoto, *Adv. Energy Mater.*, 2015, **5**, 1500096.

31 M. Klenk and W. Lai, *Phys. Chem. Chem. Phys.*, 2015, **17**, 8758–8768.

32 C. Chen, D. Chen and F. Ciucci, *Phys. Chem. Chem. Phys.*, 2015, **17**, 7831–7837.

33 W. D. Richards, T. Tsujimura, L. J. Miara, Y. Wang, J. C. Kim, S. P. Ong, I. Uechi, N. Suzuki and G. Ceder, *Nat Commun*, 2016, **7**, 11009.

34 C. Chen, Z. Lu and F. Ciucci, *Sci Rep*, 2017, **7**, 40769.

35 N. J. de Klerk, E. van der Maas and M. Wagemaker, *ACS Appl. Energy Mater.*, 2018, **1**, 3230–3242.

36 L. Kahle, A. Musaelian, N. Marzari and B. Kozinsky, *Phys. Rev. Materials*, 2019, **3**, 055404.

37 F. Ercolessi and J. B. Adams, *Europhys. Lett.*, 1994, **26**, 583–588.

38 P. Brommer and F. Gähler, *Modelling Simul. Mater. Sci. Eng.*, 2007, **15**, 295–304.

39 G. Kresse and J. Furthmüller, *Phys. Rev. B*, 1996, **54**, 11169–11186.

40 J. P. Perdew, A. Ruzsinszky, G. I. Csonka, O. A. Vydrov, G. E. Scuseria, L. A. Constantin, X. Zhou and K. Burke, *Phys. Rev. Lett.*, 2008, **100**, 136406.

41 W. G. Hoover, *Phys. Rev. A*, 1985, **31**, 1695–1697.

42 E. Akhmatskaya and S. Reich, *J. Comput. Phys.*, 2008, **227**, 4934–4954.

43 B. Escribano, E. Akhmatskaya and I. Mujika, *Cent. Eur. J. Math.*, 2013, **11**, 787 – 799.

44 E. Akhmatskaya and S. Reich, 2011, **2**, 447–462.

45 M. R. Bonilla, F. A. G. Daza, P. Ranque, F. Aguesse, J. Carrasco and E. Akhmatskaya, *ACS Appl. Mater. Interface*, 2021, **13**, 30653–30667.

46 M. R. Bonilla, F. A. G. Daza, H. A. Cortés, J. Carrasco and E. Akhmatskaya, *J. Colloid Interface Sci.*, 2022, **623**, 870–882.

47 G. Bussi, D. Donadio and M. Parrinello, 2007, **126**, 014101.

48 E. Akhmatskaya, M. Fernández-Pendás, T. Radivojević and J. Sanz-Serna, *Langmuir*, 2017, **33**, 11530–11542.

49 D. Arthur and S. Vassilvitskii, Proceedings of the Eighteenth Annual ACM-SIAM Symposium on Discrete Algorithms, USA, 2007, p. 1027–1035.

50 F. Pedregosa, G. Varoquaux, A. Gramfort, V. Michel, B. Thirion, O. Grisel, M. Blondel, P. Prettenhofer, R. Weiss, V. Dubourg, J. Vanderplas, A. Passos, D. Cournapeau, M. Brucher, M. Perrot and E. Duchesnay, *J. Mach. Learn. Res.*, 2011, **12**, 2825–2830.

51 M. Ester, H.-P. Kriegel, J. Sander and X. Xu, Proceedings of the Second International Conference on Knowledge Discovery and Data Mining, 1996, p. 226–231.

52 S. Zhang, J. Ma, S. Dong and G. Cui, *Electrochem. Energy Rev.*, 2023, **6**, 4.

53 N. M. Vargas-Barbosa and B. Roling, *ChemElectroChem*, 2020, **7**, 367–385.

54 S. A. Akbar, *Journal of Applied Physics*, 1994, **75**, 2851–2856.

55 O. Borodin, W. Gorecki, G. D. Smith and M. Armand, *J. Phys. Chem. B*, 2010, **114**, 6786–6798.

56 B. K. Wheatle, N. A. Lynd and V. Ganesan, *ACS Macro Lett.*, 2018, **7**, 1149–1154.

57 D. Rettenwander, C. A. Geiger, M. Tribus, P. Tropper and G. Amthauer, *Inorganic Chemistry*, 2014, **53**, 6264–6269.

58 D. Rettenwander, J. Langer, W. Schmidt, C. Arrer, K. J. Harris, V. Terskikh, G. R. Goward, M. Wilkening and G. Amthauer, *Chemistry of Materials*, 2015, **27**, 3135–3142.

59 R. D. Shannon and C. T. Prewitt, *Acta Crystallogr B Struct Sci*, 1969, **25**, 925–946.

60 L. Cheng, J. Park, H. Hou, V. Zorba, G. Chen, T. Richardson,

J. Cabana, R. Russo and M. Doeff, *Journal of Materials Chemistry A*, 2014, **2**, 172–181.

61 S. Yu and D. Siegel, *Chemistry of Materials*, 2017, **29**, 9639–9647.

62 C. Bernuy-Lopez, W. Manalastas, J. M. L. del Amo, A. Aguadero, F. Aguesse and J. A. Kilner, *Chem. Mater.*, 2014, **26**, 3610–3617.

63 B. Karasulu, S. P. Emge, M. F. Groh, C. P. Grey and A. J. Morris, *J. Am. Chem. Soc.*, 2020, **142**, 3132–3148.

64 R. Metzler, J.-H. Jeon, A. G. Cherstvy and E. Barkai, *Phys. Chem. Chem. Phys.*, 2014, **16**, 24128–24164.

65 B. J. Morgan, *R. Soc. open sci.*, 2017, **4**, 170824.

66 Y. Li, J.-T. Han, C.-A. Wang, H. Xie and J. B. Goodenough, *Journal of Materials Chemistry*, 2012, **22**, 15357–15361.

67 A. Logéat, T. Köhler, U. Eisele, B. Stiaszny, A. Harzer, M. Tovar, A. Senyshyn, H. Ehrenberg and B. Kozinsky, *Solid State Ionics*, 2012, **206**, 33–38.

68 X. Zhang, C. Li, W. Liu, T.-S. Oh and J. W. Fergus, *Solid State Ionics*, 2021, **369**, 115713.

69 S. Adams and R. P. Rao, *Journal of Materials Chemistry*, 2012, **22**, 1426–1434.

70 F. Chen, J. Li, Z. Huang, Y. Yang, Q. Shen and L. Zhang, *The Journal of Physical Chemistry C*, 2018, **122**, 1963–1972.

71 T. Thompson, J. Wolfenstine, J. L. Allen, M. Johannes, A. Huq, I. N. David and J. Sakamoto, *J. Mater. Chem. A*, 2014, **2**, 13431–13436.

72 M. P. O'Callaghan, A. S. Powell, J. J. Titman, G. Z. Chen and E. J. Cussen, *Chem. Mater.*, 2008, **20**, 2360–2369.

73 Y. Li, J.-T. Han, C.-A. Wang, H. Xie and J. B. Goodenough, *J. Mater. Chem.*, 2012, **22**, 15357–15361.